# Electric Field Directed Self-Assembly of Cuprous Oxide Nanostructures for Photon Sensing

**Sangeeta Sahoo,[†,¶,*] Sudhir Husale,[‡,£] Bryant Colwill,[§] Toh-Ming Lu,[§] Saroj Nayak,[⊥] and Pulickel M. Ajayan[∥]**

[†]Department of Materials Science and Engineering, Rensselaer Polytechnic Institute, Troy, New York 12180, [‡]Rowland Institute at Harvard, Harvard University, 100 Edwin H. Land Boulevard, Cambridge, Massachusetts 02142, [§]Center for Integrated Electronics, Rensselaer Polytechnic Institute, Troy, New York 12180, [⊥]Department of Physics, Applied Physics and Astronomy, Rensselaer Polytechnic Institute, Troy, New York 12180, and [∥]Department of Mechanical Engineering and Materials Science, Rice University, Houston, Texas 77005. [¶]Present address: Laboratory of Nanoscale Electronics and Structures, School of Engineering, Ecole Polytechnique Fédérale de Lausanne, Station-17, Ch- 1015, Switzerland. [£]Present address: Laboratory of Nanostructures and Novel Electronic Materials, School of Engineering, Ecole Polytechnique Fédérale de Lausanne, Station-17, Ch- 1015, Switzerland.

**ABSTRACT** We demonstrate a novel chemical-free water-based technique to synthesize various forms of cuprous oxide nanostructures at room temperature. The self-assemblies of these nanostructures are formed by the anodic oxidation of Cu in deionized (DI) water. Direct growth of these nanostructures on $SiO_2$/Si (100) substrate has been successfully achieved by tuning the bias voltage and the growth duration. A variety of nanostructures from one-dimensional nanowires to different complex two- and three-dimensional structures are successfully grown by this method. We show that the morphological evolution in the self-assembly of the structures strongly depends on the spatial electric field distribution on the substrate. Furthermore, the electrical devices made from these nanowire networks exhibit promising photon sensing characteristics under white light illumination and can be exploited for future applications in photodetection and photovoltaic studies at the nanoscale level.

**KEYWORDS:** electrodeposition · self-assembly · nanostructures · photodetectors

From fundamental study through technological application, nanomaterials have garnered unprecedented attention due to their strikingly different properties at nanolevel dimensions as compared to the nature of its bulk counterpart. Further, the complex structural varieties enhance additional functionalities in various species of nanomaterials like nanowires, nanoparticles, nanocrystals, nanorods, nanocubes, nanoflowers *etc.* since the size, shape, and morphological features influence the electrochemical and physical properties of nanostructures.[1] Controlled execution of these features makes any material an attractive and promising building block for advanced technological applications. Therefore, it is very challenging and important to have complete control over the size distribution, the shape evolution, and the crystalline structure of the materials. Synthesizing such novel nanostructures and implementing them into various exciting applications have been a major field of research in the past decade.

In particular, semiconducting nanomaterials have been considered as the focal point of the field of optoelectronic research and technology for decades due to the beauty and diversity in their electronic band structure.[2] Among the conventional semiconducting materials, cuprous oxide ($Cu_2O$) is known to be one of the earliest semiconducting materials with a relatively low band gap of order ~2 eV.[3] As a consequence of its superior optoelectronic properties, nontoxic nature, natural abundance, simplicity in the synthesis procedures, and inexpensive market value, $Cu_2O$ has been used extensively to resolve several energy-related problems from solar energy conversion to hydrogen production by photocatalysis of water.[4−7] The enhanced electrochemical reactivity in $Cu_2O$ nanomaterials initiates its use as the negative electrode material for Li-ion-based batteries.[8] The antifouling and algicidic properties[9] along with photon absorption capabilities make $Cu_2O$ material a very important base element for biological and medical applications. Recently, an enhancement in photocurrent for dendritic branched n-type $Cu_2O$ has been reported.[10] Apart from the technological importance, $Cu_2O$ materials offer the opportunity to study fundamental physical phenomena like Bose−Einstein condensation at low temperature[11,12] due to the large excitonic binding energy with long lifetime and the electron−electron correlation effects on the electronic structure of the high-temperature cuprate-based superconductors.

*Address correspondence to sangeeta.sahoo@epfl.ch.

Received for review August 2, 2009 and accepted November 2, 2009.

**Published online November 10, 2009.**
10.1021/nn900915m CCC: $40.75

In view of the great potential importance of $Cu_2O$ nanomaterials, it is necessary to have a generic synthesis process which can have control over the size distribution, the shape evolution, and the crystalline structure of the materials in a very efficient way in order to exploit these additional functionalities into various successful applications at the nanoscale level. There have been several approaches, from complex electrochemical reaction to thermal annealing, employed for the synthesis of copper oxide nanowires.[13] Solution-based electrochemical synthesis of $Cu_2O$ nanoparticles,[4,14−19] nanowires,[20] nanospheres,[21] and nanocubes[22,23] has been reported previously.[24−26] Nevertheless, among liquid-based techniques, electrodeposition is the most popular and simplest synthesis methodology. It gets even easier and simpler when deionized (DI) water serves as the effective electrolyte instead of hazardous inorganic and/or organic chemical solvents. Furthermore, a synthesis process that can directly integrate the functional nanomaterials on any desired substrate for the implementation of successful device applications is much more attractive and advanced than that of solution-based nanomaterials. Here, we demonstrate such a simple room-temperature-based synthetic approach to prepare various $Cu_2O$ nanostructures including very thin nanowires directly on the substrate.

In this study, we illustrate a catalyst-free, template-free, nontoxic, low-cost, highly reproducible, one-step synthesis process which can lead to a generic technique to prepare various metal/metal oxide nanostructures directed by the electric field. A simple anodic oxidation of various active metals in DI water is the center point of this method. By employing Cu as the active anode material and DI water (resistivity ~18 MΩ · cm) as the effective electrolyte, we present a standard process to synthesize $Cu_2O$ nanostructures in various forms and shapes directly on the substrate. Depending on (i) the potential between the cathode and anode, (ii) the time duration of the applied bias, and (iii) the spatial dependence of the effective electric field, different nanostructures are formed. From 1-D nanowire geometry to 2-D and 3-D nanowire-based matrix structures are synthesized directly on glass and $SiO_2$/Si substrates. The nanowires can have diameters in the sub-10-nm range and a length in the range of 100−400 nm. In addition to the synthesis, we explore the current−voltage ($I$−$V$) characteristics of different $Cu_2O$ nanowire networks (area ~0.5−2 μm$^2$). These measurements were carried out on different density networks in both dark and white light illumination conditions. The results indicate that the devices are sensitive to the photon exposure and yield very low dark current.

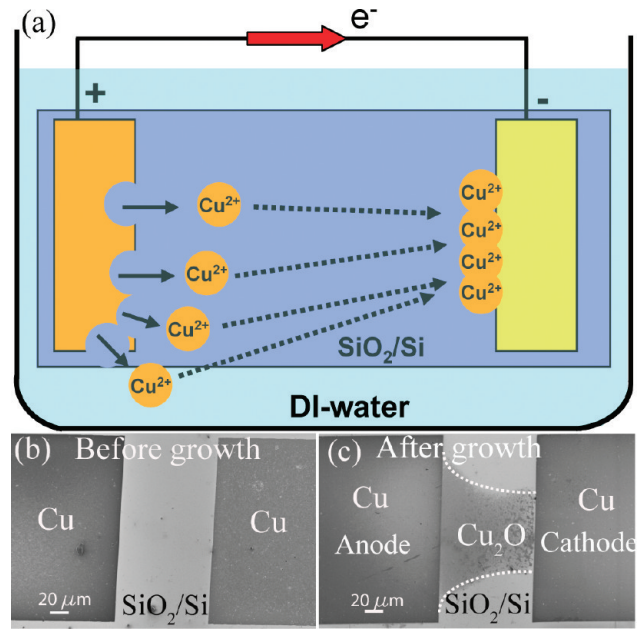


**Figure 1. (a) Schematic representation of the experimental setup and the synthesis process. (b) FESEM micrograph of an as-fabricated setup with two Cu electrodes on the $SiO_2$/Si surface before growth. (c) FESEM micrograph representing the condition after growth. The region between the electrodes, marked with the white dotted lines, indicates the growth region on the substrate.**

## RESULTS AND DISCUSSION

Figure 1a represents a schematic of the basic setup and the synthesis process. The cell contains two electrodes defined on a solid substrate immersed in DI water. The electrodes are connected to an external electric power supply. On application of an external electric field, copper oxidizes to cupric ions at the anode (anode: $Cu \rightarrow Cu^{2+} + 2e^-$) and electrochemical reduction happens for water at the cathode surface (cathode: $2H_2O + 2e^- \rightarrow H_2 + 2OH^-$). A threshold voltage to initiate the growth of the nanostructures is expected, as a minimum potential must be provided to reach the copper electro-oxidation and water reduction processes at the anode and cathode, respectively. Higher electric field accelerates the release of the copper ions from the anode and simultaneously causes an increased electrophoretic force pushing those ions toward the cathode.[27] Near the cathode, copper ions combining with $OH^-$ ions form $Cu_2O$ molecules which act as the building blocks for the self-assembly of $Cu_2O$ nanostructures ($2Cu^{2+} + 2OH^- \rightarrow Cu_2O\downarrow + H_2O$). The growth starts from the cathode surface and continues to cover the interspace between the two electrodes with time.

Figure 1b,c represents the FESEM micrographs of a sample cell before and after the growth of $Cu_2O$ nanostructures, respectively. The as-fabricated sample geometry is shown in Figure 1b. After the fabrication of electrodes, we immerse the sample in DI water and apply an electric field through the electrodes externally. In Figure 1c, we show a sample subsequently removed from the DI water following the growth of $Cu_2O$ nanostructures on the substrate. Depending on the electric

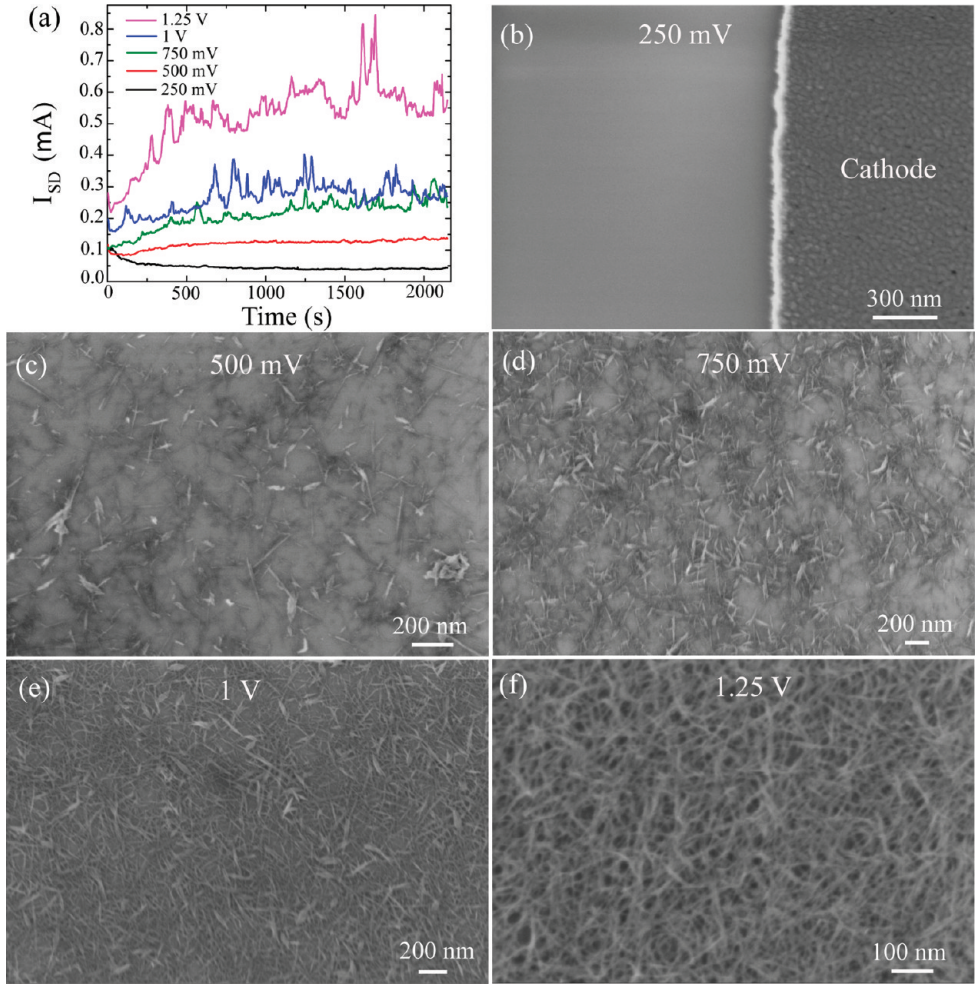


**Figure 2. (a) Collection of current *vs* time curves at different voltages applied to a set of samples prepared at the same condition. (b−f) Corresponding SEM micrographs of the samples after taken out of the water. (b) Image showing the region with highest probability of growth, *i.e.*, the region close to the cathode. No growth was observed at 250 mV bias for the duration of about 36 min. (c−f) Images showing the regions chosen from the center part of the interelectrode spacing on the substrate.**

field intensity, we vary the growth duration. As an example, we applied a bias of 500 mV for about 36 min to get the sample shown in Figure 1c. A clear difference appears at the region between the electrodes in Figure 1b versus that of Figure 1c, due to the growth of the nanostructures. In Figure 1c, the region marked by the white dotted lines indicates the region of growth. The image also indicates that the growth starts at the closest center point on the cathode surface from anode.

Now, we present the effects of the bias voltage on the nanostructure synthesis process illustrated in Figure 2. We have measured the current as a function of time during the growth for different voltages from 250 mV to 1.25 V. In Figure 2a, we have displayed a collection of current *versus* time curves for all of the samples shown in Figure 2b−f at different voltages. All of the samples had the same geometry. Since the electrodes were not connected, the current was mainly carried by the ions present in the DI water. With increasing voltage, the current increases systematically. The black and red curves represent the currents at 250 and 500 mV, respectively. The transient characteristics of the black and red curves differ only at their initiation stage. As the time progresses, except for the magnitude, the characteristics of the two curves remain quite similar. The green curve represents the current variation with time for the bias of 750 mV. The overall current increases as the bias increases from 500 to 750 mV. Furthermore, there are some variations in the green curve than that appears in the red curve at saturated parts. These fluctuations indicate that there are ions coming out from the anode time to time and contribute to the current. The fluctuations appear more frequently with higher amplitudes as we increase the bias from 750 mV to 1.0 V (the blue curve) and to 1.25 V (the magenta curve). Interestingly, the amplitude difference in the overall current is much higher when we go from 1.0 to 1.25 V than that from 750 mV to 1.0 V. This is mainly because at 1.23 V electrolysis of water starts at the anode surface. The ions coming from the electrolysis of water along with the increased copper ions from the anode increase the overall current at a much higher level.

The FESEM micrographs representing each of those samples with the current−time characteristics presented in Figure 2a are shown in Figure 2b−f. At 250 mV bias, no growth is observed, as shown in Figure 2b. No growth appeared near the surface of the cathode where the growth is highly probable, indicating that the applied bias is not enough to start the process. This is obvious since a threshold voltage is needed to oxidize and release the copper ions from the anode. At higher bias with 500 mV (Figure 2c), we observe some scattered nanostructures between the electrodes on the substrate. With increasing voltage up to 750 mV, we observe higher density of the nanostructures (Figure 2d), which is consistent with the higher current presented in Figure 2a. Except for the density of the nanostructures, we do not observe any distinguishable differences between the images displayed in Figure 2c,d. At 1 V, in Figure 2e, there is more coverage on the substrate with the nanostructures than that in Figure 2c,d. Finally, in Figure 2f, at 1.25 V bias, we observe a very dense coverage of the nanostructures containing a random orientation of $Cu_2O$ nanowires having diameter in the sub-10-nm range and void spaces. With the geometry mentioned above for this study, with 1.25 V bias applied for 36 min, we get a uniform 2-D network of nanowires. Increasing the growth duration, one can create a 3-D nanowire matrix medium. The duration of the growth presented in Figure 2 is about 36 min for all of the samples. Note, all the images from Figure 2c−f are collected from the middle part of the substrate between the electrodes.

Apart from the bias dependence of the growth process, we have investigated the effect of the effective spatial electric field distribution between the electrodes and the duration of the growth. In Figure 3, we have presented a collection of FESEM micrographs of nanostructures with variations in structural morphology. We have made a sketch of different regions presenting different electric field distribution between the electrodes under an applied bias. The regions presented by different color code are named numerically as shown in Figure 3a. In the inset (Figure 3a), we show the SEM image of a sample after the growth of nanostructures on the surface. The growth area indicated by the dotted elliptical region in the inset resembles the sketch drawn based on the electric field distribution (Figure 3a) in a realistic way. Obviously, different regions represent different effective electric fields which govern the growth process and the self-assembly of the structures in different ways at different places. In Figure 3b−o, we display FESEM images of different nanostructures grown on different regions (marked with the representative colored zone) of the substrate with different growth conditions. Figure 3b−h represents various morphologically different nanostructures grown at different zones with 1 V bias applied for 50 min.

The nanostructures formed near the cathode (zone 1) and the anode surfaces (zone 3) are shown in Figure 3b,c. In Figure 3b, we observe a similar type of nanowire network as shown previously in Figure 2f with 1.25 V for 36 min. Therefore, a similar type of nanostructure pattern as shown in Figure 3b and Figure 2f can be formed by varying the electric field and the growth duration since the growth rate depends on the electric field. On the other hand, we observe a clear difference in the density and the diameter of the nanowires shown in Figure 3b,c. Near the cathode, we observe a highly dense network containing a much thinner nanowire (diameter ~5 nm), whereas near the anode, we observe that a low density network contained relatively thicker nanowire structures. The higher nanowire density near the cathode indicates that the ions after releasing from the anode travel toward the cathode due to the electrophoretic force. At the transverse direction from the boundary region (the gray zone, *i.e.*, zone 7) to the center of the interelectrode spacing (the green zone, *i.e.*, zone 2), the product of various nanostructures is shown in Figure 3d−f. At the boundary zone of the growth, we find nanoflake-like structures which are scattered on the substrate, as shown in Figure 3d. As we come closer to the center of the interelectrode spacing, a higher density of the nanostructures (nanowires and nanoflakes) appears. The nanowires start to self-assemble into a thicker nanowire followed by the formation of the flower-like pattern on top of the initial layer of the nanowire mat, as shown in Figure 3e. At the middle part (the green region in Figure 3a) of the space between the electrodes where the electric field is supposed to be uniform, we observe mainly a mixture of two types of structures: (i) nanowires and (ii) nanoleafs as shown in Figure 3f. At zone 6, that is, a little inside from the boundary region to the core region of the growth, we observe flower-like multiwing structures branched out from the center, as shown in Figure 3g. These branched nanowire-based structures are very similar to those presented in Figure 3e except for the additional layer underneath indicating a higher density growth toward the interelectrode spacing. Finally, at the corner of the electrodes where the electric field is supposed to be stronger than any other places, more flower-like structures form on top of an initial layer of 2-D nanowire medium (Figure 3h,i). In the insets of Figure 3h, we display the magnified image of two nanoflowers shown in Figure 3h. In Figure 3i, we present the SEM image of a part of the anode along with the surrounding region which contains a low density nanowire layer nicely topped with many nanoflowers, as shown in the inset. The applied bias was 750 mV, and the branches of the flowers are shorter than that presented in Figure 3e,g,h.

However, with a higher bias of 1.5 V, the sacrificial anode was observed to disappear within 15 min to form the nanostructures shown in Figure 3j. After the

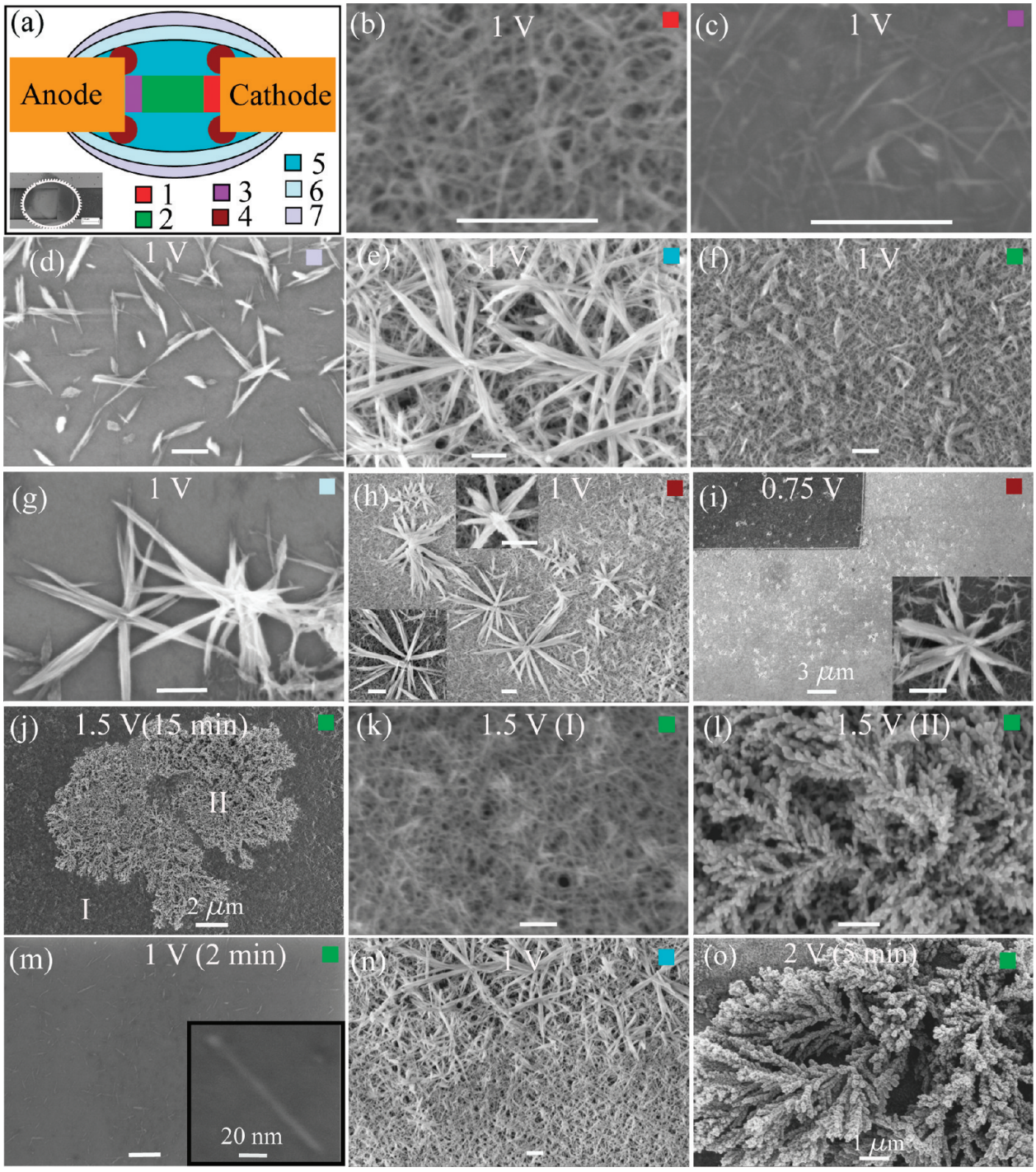


**Figure 3. Various $Cu_2O$ nanostructures grown with different conditions on the substrate. (a) Schematic presentation of the different growth zones depending on the electric field distribution between the electrodes. Inset: SEM image of a sample after growth with dotted lines indicating the growth region. (b−h) Different nanostructures grown on different regions (indicated by the colored zone numbers) on the substrate with a bias of 1 V applied for 50 min. (i) SEM image showing the growth at the corner region (zone 4) with a bias 750 mV applied for 50 min. Inset: magnified image of the flower-like structures which appear as scattered points in (i). (j) Two different set of structure (I and II) formation due to a bias of 1.5 V for 15 min. (k,l) Magnified images of the type I and type II structures (shown in j), respectively. (m−o) SEM images showing from 1-D single nanowires to 2-D nanonetwork up to 3-D dendritic structures, respectively, depending on the applied bias and the growth duration. The scale bar is 200 nm or otherwise as mentioned in the images.**

formation of an initial coating with nanowires, a second layer containing 3-D dendrite-like structures is observed. For a clear understanding, we have displayed those two sets of structures (I and II in Figure 3j) separately in Figure 3k,l, respectively. The first set of structures (Figure 3k) resembles the similar type of network as presented in Figure 3b and Figure 2f. The second set clearly represents the formation of polycrystalline 3-D tree-like pattern structures with higher bias. Finally,in Figure 3m−o, we present the structural evolution from

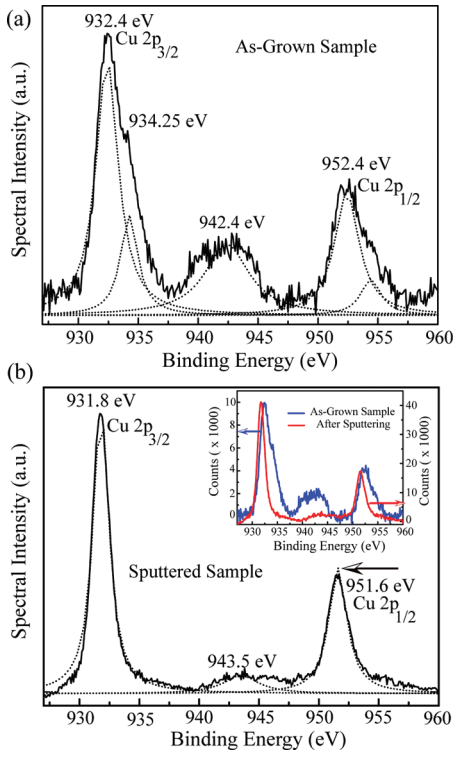


**Figure 4. (a) Core-level X-ray photoelectron spectra of $Cu_{2p}$ from as-grown nanowire sample deposited directly on a glass substrate. The peak-fit reveals a main peak at 932.4 eV for Cu $2p_{3/2}$ accompanied by other higher binding energy satellite peaks at 934.25 and 942.4 eV. (b) XPS spectra of the same sample after sputtering with a removal of ~5 nm from the surface of the sample. The peak-fit indicates only the main peaks at 931.8 eV for Cu $2p_{3/2}$ and at 951.6 eV for Cu $2p_{1/2}$. Inset: Comparison between the XPS spectra for the ss-grown and sputtered sample.**

a single 1-D nanowire to 2-D nanowire network up to 3-D tree-like dendritic structure formation by varying the electric field and the growth time. A randomly oriented network of well-separated individual $Cu_2O$ nanowires has been successfully achieved (shown in Figure 3m) by applying 1 V for 2 min. The individual nanowires are very important for the exploration of the fundamental electrical and optical properties at the 1-D limit. Two-dimensional nanonetwork (Figure 3n) and 3-D matrix (Figure 3k) can be also formed by this method for thin film application and for potential use in biological systems. Moreover, when we increase the bias up to 2 V, within 5 min, the anode dissolves into 3-D patterns, as shown in Figure 3o. However, the mechanism of 3-D pattern formation is also important to study the growth at relatively higher voltages as indicated in Figure 3l,o.

In order to determine the oxidation phase and the surface characteristics of the nanostructures, we have acquired core-level XPS spectra from the nanowire sample grown with a bias of 1 V for 70 min on a glass substrate. Figure 4a presents the XPS spectrum of $Cu_{2p}$ for the as-grown sample. The spectrum is corrected with reference to the $C_{1s}$ peak at 284.6 eV. The peaks at 932.4 and 952.4 eV can be addressed to the binding energy of Cu $2p_{3/2}$ and Cu $2p_{1/2}$, respectively.[20] From the peak-fit for the Cu $2p_{3/2}$, we observe two extra satellite peaks appearing on the higher binding energy side, 934.25 and 942.4 eV along with the main peak at 932.4 eV. Since the 3d shell is expected to be completely filled in $Cu_2O$, the shake up satellite peaks indicate the presence of an unfilled Cu $3d^9$ shell, that is, the existence of CuO at the surface.[4,28]

The existence of CuO phase in the as-grown sample could be explained either by the surface oxidation in ambient condition or by the core−shell-type of structures of $Cu_2O$ nanowires with CuO as the capping surface layer.[29] Since the sample was exposed for a long time in ambient conditions before the XPS spectra were taken, the surface oxidation cannot be ignored. In order to get a cleaner surface, we have sputtered to remove ~5 nm from the surface of the sample. The XPS spectrum of the sputtered sample is shown in Figure 4b. The Cu $2p_{3/2}$ peak has been now moved to 931.8 eV, and notably, there is no satellite peak accompanied with this main peak. This indicates that most of the surface layers containing CuO phase for the as-grown sample (Figure 4a) are removed by the sputtering. Still, the broad satellite peak around 943.5 eV indicates a weak presence of CuO even after the sputtering. For a clear difference, we have presented the XPS spectra for the as-grown sample and the sputtered sample in the inset of Figure 4b. It is clear that sputtering significantly removes the $Cu^{2+}$ phase from the sample. It has been also reported that $Cu_2O$ can be easily covered by a relatively more stable CuO surface layer.[30] Moreover, the relative higher intensity of the $Cu_2O$ phase in Figure 4a indicates the main contribution to the nanowires is from $Cu^+$. From the XPS analysis, we can conclude that the nanowires are mostly of $Cu_2O$ phase. However, CuO phase might also be present as the capping layer. A detailed study of the oxidation phase of the nanowires is necessary and under consideration for future studies.

In order to study the electrical properties, we have fabricated two microelectrodes (length ~3.2 μm, width ~500 nm) on top of the nanowire network in metal−semiconductor−metal (MSM) geometry. For each device, both the metal−semiconductor contacts are symmetric and we have also observed symmetric *I*−*V* characteristics for all of the devices. Electrodes are defined by electron beam lithography followed by an e-beam deposition of ~100 nm of Au on top of ~5 nm of Ti. The nanowires were grown with 1 V bias applied for 50 min for all four samples. In Figure 5a−d, we have displayed SEM micrographs of four such MSM devices having channel lengths (*i.e.*, the spacing between the electrodes) of 210, 260, 580, and 720 nm, respectively. Depending on the interelectrode spacing, we have categorized those four devices into two sets. Set I contains sample-1 and sample-2, and set II consists of sample-3 and sample-4. Besides the channel length, the SEM images indicate that sample-1 and sample-2

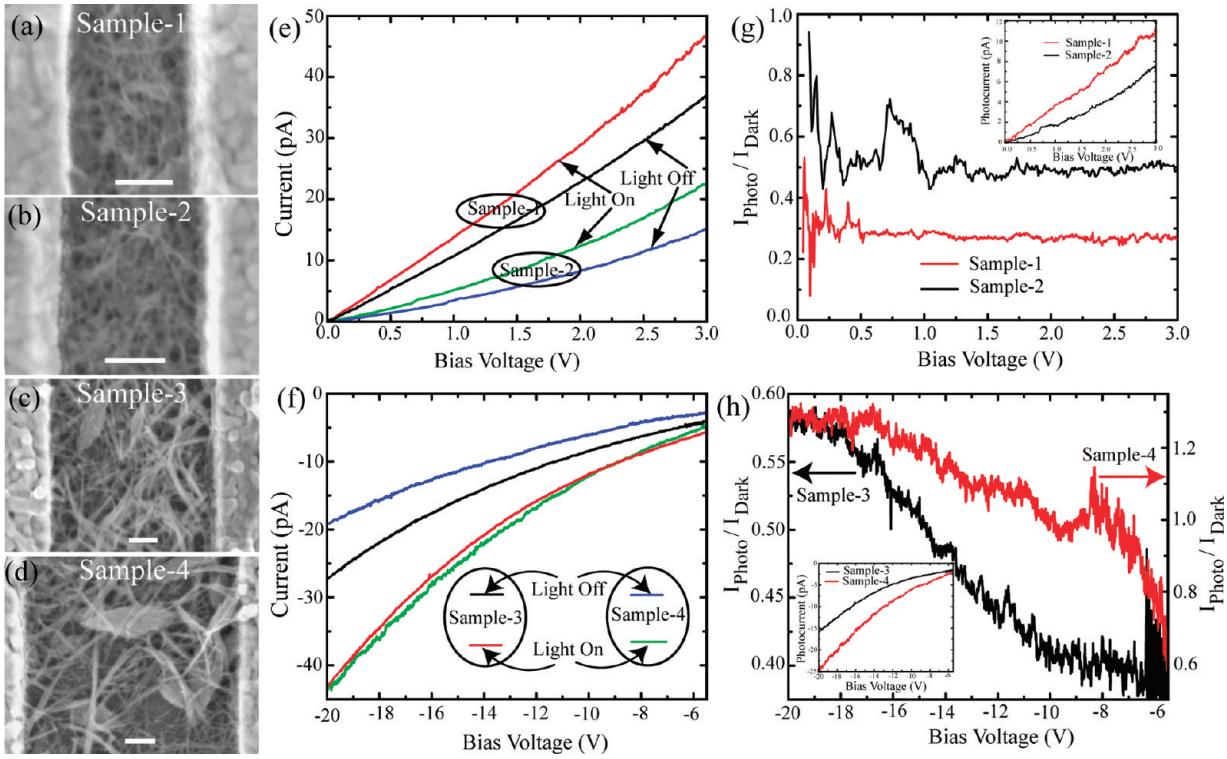


**Figure 5. (a−d) SEM micrographs of $Cu_2O$ nanowire devices having electrode spacings of 210, 260, 580, and 720 nm, respectively. The electrodes are 3.2 μm wide for all of the devices. The scale bar is 100 nm. The current−voltage (*I*−*V*) measurements are carried out at dark and under illumination conditions for all four samples. Depending on the interelectrode spacing, the samples are categorized into two sets, *viz.* set I: sample-1 and sample-2; set II: sample-3 and sample-4. (e,f) *I*−*V* characteristics of set I and set II, respectively. (g,h) Plot of the ratio of photocurrent ($I_{photo}$) to the dark current ($I_{dark}$) *vs* bias voltage for set I and set II, respectively. Insets of (g) and (h) represent the photocurrent as a function of bias for set I and set II, respectively.**

comprise similar density nanowire films, whereas the density of nanowires in sample-3 is more than that of sample-4. Note, the difference in the densities for sample-3 and sample-4 for the selected area, as presented here, is not clear, but for the whole area of the devices, the difference was noticeable. In order to investigate the feasibility of a $Cu_2O$ nanowire-based MSM photodetector, we have carried out *I*−*V* measurements on those four samples under white light illumination and under room darkening conditions. The *I*−*V* characteristics, in both dark and illuminated conditions, for set I (*i.e.*, for sample-1 and sample-2) and set II (*i.e.*, for sample-3 and sample-4) are displayed in Figure 5e,f, respectively. Since the contacts are symmetric, we selectively present the *I*−*V* characteristics for set I in the positive bias and for set II in the negative bias direction. For set II, at $|V_b| \leq 5$ V, the current was at the noise level, and hence, we measured the *I*−*V* characteristic above |5 V| (Figure 5h). The corresponding current densities in mA/cm$^2$ for these four devices are shown in the Supporting Information.

As the channel length increases from 210 nm for sample-1 to 260 nm for sample-2 in set I (from 580 nm for sample-3 to 720 nm for sample-4 in set-II), the dark current decreases from the black curve to the blue curve in Figure 5e (Figure 5f). Figure 5e,f also shows a higher current under illumination conditions (the red and the green curves) than in the dark (the blue and black curves) for all four devices. The corresponding photocurrent−voltage curves, which can be deduced by subtracting the dark current from the current under illumination for all devices, are presented in the insets of Figure 5g,h. Note, we have observed that the samples are very stable with respect to their photosensitivity over time when they are stored under moderate vacuum conditions.

In general, the MSM devices can be considered as two back-to-back Schottky diodes, one of which can be considered as forward-biased and the other one as reverse-biased. Under a high applied bias, the total dark current through the devices will be controlled by the reverse-biased Schottky thermionic emission current as[31]

$$I_{dark} = AA^*T^2e^{-q\phi_{B_{eff}}/kT} = AA^*T^2e^{-q(\phi_B-\Delta\phi)/kT} \quad (1)$$

where *A* is the surface area of the photodetection region between the metal electrdes, $A^*$ is the Richardson constant, *q* is the electronic charge, $\phi_{B_{eff}}$ is the effective barrier height, $\phi_B$ is the Schottky barrier height at the metal−semiconductor interface, *k* is the Boltzmann constant, *T* is the absolute temperature, $\Delta\phi = ((qE)/(4\pi\varepsilon))^{1/2}$ is the image force induced lowering in the barrier height due to the applied electric field *E*, and *e* is the dielectric constant of the semiconducting material.

The electric field, $E$, can be calculated as $V/L$, where $V$ is the applied bias voltage and $L$ is the spacing between the electrodes.[32] Nevertheless, the $I-V$ characteristics shown in Figure 5e,f do not saturate at high bias voltage but slowly increase with increasing bias, confirming the barrier height lowering for the devices due to the applied electric field.

Under illumination with higher energy than the band gap of the semiconducting material, electron−hole pairs are generated due to the absorption of photons, and hence the carrier density increases inside the material. There is a net photocurrent flow through the detector if the photogenerated carriers can reach the electrodes before they recombine inside an active region of the material. Furthermore, an electric field can accelerate the carriers to reach the electrodes before their recombination, resulting in a higher photocurrent. The occupancy of the interface levels also changes due to the illumination at the interface causing a re-adjustment of the space-charge region hence the barrier height at the interface.[33] However, in steady state under constant illumination, the photocurrent ($I_{photo}$) is proportional to the electron−hole pair generation rate and is given by[32]

$$I_{photo} = \frac{A_{NW}}{A_{Exp}}(1 - R)(1 - e^{-\alpha d})\frac{\eta.qP_{Opt}}{h\nu} \qquad (2)$$

where $A_{NW}$ is the active area covered with the nanowires between the electrodes, $A_{Exp}$ is the total area between the electrodes exposed to the illumination, $R$ is the reflectivity, $\alpha$ is the absorption coefficient, $d$ is the thickness of the nanowire matrix, $\eta$ is the quantum efficiency, that is, the number of electron−hole pairs generated per incident photon, $h\nu$ is the photon energy, and $P_{Opt}$ is the optical power of the incident light.[32] Since in the experimental study we used the same light source with same conditions for all of the devices, the channel length and the nanowire density take control over the photocurrent. The photocurrents for set I and set II are shown in the insets of Figure 5g,h, respectively. For all of the samples, the slow increase in the photocurrent with increasing bias indicates that the photocurrent is controlled by the effective barrier height at the interfaces. We observe a higher photocurrent for sample-1 than sample-2 in set I. Although the spacing and hence the area between the electrodes for sample-1 is smaller than that for sample-2, the increased photocurrent at relatively low voltage indicates that there might be a slightly higher density of nanowires for sample-1 as compared to sample-2. However, the average length and the orientation of the nanowires in the devices also influence the overall transport through the device. A fraction of photocurrent is also expected to be lost due to recombination in the longer active channel devices. Unlike the set I, in the inset of Figure 5h, we observe a higher photocurrent (the red curve) for sample-4 (longer spacing) than sample-3 (the black curve) even though the nanowire density was much lower in sample-4 compared to sample-3 (Figure 5c,d). This definitely indicates that the higher surface area absorbs much more photons and hence yields an increase in photocurrent. It is important to note that the nanowires are mostly less than 500 nm long, and hence the devices in set II possess multiple cross-junctions connected by the nanowires between the electrodes. Each of these nanowire junctions faces interfacial barriers, which reduce the overall current as seen for the samples in set II. With multiple cross-junction-based devices, transport is controlled not only by the barrier height at the metal−semiconductor interface but also by the tunneling barrier at each cross-junction. However, under direct illumination on each of these cross-junctions, the tunneling of the carriers through the junctions can be enhanced as it is indicated by the higher photocurrent for the longer spacing sample (sample-4) in the inset of Figure 5h.

In addition to the photocurrent, the ratio of photo-to-dark current (*i.e.*, $I_{photo}/I_{dark}$) is an important parameter to evaluate the performance of the detector as an optically controlled electronic switch.[34] We have displayed the $I_{photo}/I_{dark}$ ratio for set I and set II samples in Figure 5g,h, respectively. In the similar current range, we observe that for the samples in set I the $I_{photo}/I_{dark}$ ratio almost stays independent of the bias voltage, whereas for the samples in set II the $I_{photo}/I_{dark}$ ratio shows a strong voltage dependence. The constant $I_{photo}/I_{dark}$ ratios for sample-1 and sample-2 (in Figure 5g) indicate that both the photocurrent and the dark current vary in a similar way with bias. In this case, since the channel lengths of the devices are within the range of the nanowire length, we can neglect the tunneling effect and hence the transport is dominated by the Schottky thermionic emission. For the case of longer spacing devices as in set II (Figure 5h), the $I_{photo}/I_{dark}$ ratio increases with bias initially and saturates at higher voltages for both of the samples. Due to the presence of multi-cross-junctions in these samples, in addition to the Schottky thermionic emission, the tunneling takes a demanding role up to certain voltage (below the onset of the saturation), and we observe an increasing photo-to-dark current ratio. Obviously, the saturation voltage depends on the optical power and the density of the nanowire. In this case, the effect of the disorder on the transport should also be considered as it has been reported for the disordered molecular systems.[35]

## CONCLUSION

In conclusion, we have demonstrated a novel simple route to synthesize various interesting nanostructures of $Cu_2O$ directly on Si substrates. The synthesis route described in this study is based on the electric field distribution on the substrates between two metal electrodes. This intriguing technique is

room-temperature-based, liquid phase, low-cost, highly reproducible, simple, and new route to synthesize various transition metal oxide nanostructures. Using this route, we have been able to synthesize well-separated individual $Cu_2O$ nanowires, two-dimensional nanowire networks, and three-dimensional matrix nanonetworks in desirable packing densities directly on the substrate. Finally, the results on the electrical property of $Cu_2O$ nanowire-based MSM devices show a very low dark current which drastically diminishes the current noise and enhances the photo-to-dark current ratio.[36] The photocurrent can be enhanced by removing the surface layer of CuO. Furthermore, the detector channel length influences the photocurrent and bias dependence of the $I_{photo}/I_{dark}$ ratio. These devices show promise toward lowering the dark current and hence increasing the detector performance.

## EXPERIMENTAL METHODS

**Synthesis of $Cu_2O$ Nanostructures:** We used Si (100) substrate with thermally oxidized $SiO_2$ (thickness ~100 nm) as the top dielectric layer for the growth of $Cu_2O$ nanostructures. In addition to $SiO_2$/Si, $Si_3N_4$/Si and glass slides were also used as substrates for the growth, and we do not observe any distinguishable differences in the nanostructures. At first, two Cu electrodes (area $\sim 300 \times 100\ \mu m^2$), separated by a distance of 100 μm, were fabricated on the $SiO_2$/Si substrate. The electrodes were patterned *via* electron beam lithography and/or mid-UV contact lithography followed by an e-beam deposition of Cu (thickness ~100 nm). We used Karl Suss Microprobe station to connect the electrodes to the external power supply from a Keithley 4200 source measure unit. We used DI water (7.5 mL; resistivity ~18 MΩ · cm) as the electrolyte for the synthesis. We employed Supra-55 for field emission scanning electron microscope (FESEM) imaging. We have characterized the materials by X-ray photoelectron spectroscopy (XPS). XPS spectra were acquired in PHI 5400 instrument using a Mg Kα probe beam.

**Device Fabrication and Electrical Measurements:** After the synthesis of the nanostructures, we have contacted a small area (in the range of 0.5−2 $\mu m^2$) of nanowire network by two metal electrodes. In these devices, the density of the nanostructures was varied by selecting different regions on the substrates as explained in Figure 3. Electrical measurements are carried out with the same Keithley 4200 source measure unit at dark conditions and under white light illumination. A 100 W light bulb was used as the white light source, and the light was focused through a microscope objective lens above the surface of the samples. We have calibrated the illuminance of the light falling on the surface of the samples by an illuminance meter (Model P30SC0, LMT). The measured illuminance was about 3.8 klx, while the ambient in-door light illuminance referred as the dark condition was 0.25 klx.

*Acknowledgment.* Financial support received from RPI, the IFC New York at RPI, Army Research Lab, and the NSF NSEC to pursue this work is acknowledged. The authors thank Drs. K. Chinnathambi, H. Li, and R. Planty for their help in determination of the oxidation phase of the nanostructures. The authors acknowledge Mr. A. Bierman for his help in the calibration of the light source.

*Supporting Information Available:* Normalized photocurrent data in mA/cm$^2$ for all four devices. This material is available free of charge *via* the Internet at http://pubs.acs.org.

## REFERENCES AND NOTES

1. Yin, Y.; Alivisatos, A. P. Colloidal Nanocrystal Synthesis and the Organic−Inorganic Interface. *Nature* **2005**, *437*, 664–670.
2. Lieber, C. M.; Zhong, L. W. Functional Nanowires. *MRS Bull.* **2007**, *32*, 99–104.
3. Shen, M. Y.; Yokouchi, T.; Koyama, S.; Goto, T. Dynamics Associated with Bose−Einstein Statistics of Orthoexcitons Generated by Resonant Excitations in Cuprous Oxide. *Phys. Rev. B* **1997**, *56*, 13066–13072.
4. Yin, M.; Wu, C.-K.; Lou, Y.; Burda, C.; Koberstein, J. T.; Zhu, Y.; O'Brien, S. Copper Oxide Nanocrystals. *J. Am. Chem. Soc.* **2005**, *127*, 9506–9511.
5. Nian, J.-N.; Hu, C.-C.; Teng, H. Electrodeposited p-Type $Cu_2O$ for $H_2$ Evolution from Photoelectrolysis of Water under Visible Light Illumination. *Int. J. Hydrogen Energy* **2008**, *33*, 2897–2903.
6. Hara, M.; Kondo, T.; Komoda, M.; Ikeda, S.; Shinohara, K.; Tanaka, A.; Kondo, J. N.; Domen, K. $Cu_2O$ as a Photocatalyst for Overall Water Splitting under Visible Light Irradiation. *Chem. Commun.* **1998**, 357–358.
7. de Jongh, P. E.; Vanmaekelbergh, D.; Kelly, J. J. $Cu_2O$: A Catalyst for the Photochemical Decomposition of Water? *Chem. Commun.* **1999**, 1069–1070.
8. Poizot, P.; Laruelle, S.; Grugeon, S.; Dupont, L.; Tarascon, J.-M. Nano-Sized Transition-Metal Oxides as Negative-Electrode Materials for Lithium-Ion Batteries. *Nature* **2000**, *407*, 496–499.
9. Li, X.; Tao, F.; Jiang, Y.; Xu, Z. 3-D Ordered Macroporous Cuprous Oxide: Fabrication, Optical, and Photoelectrochemical Properties. *J. Colloid Interface Sci.* **2007**, *308*, 460–465.
10. McShane, C. M.; Choi, K.-S. Photocurrent Enhancement of n-Type $Cu_2O$ Electrodes Achieved by Controlling Dendritic Branching Growth. *J. Am. Chem. Soc.* **2009**, *131*, 2561–2569.
11. Johnsen, K.; Kavoulakis, G. M. Probing Bose−Einstein Condensation of Excitons with Electromagnetic Radiation. *Phys. Rev. Lett.* **2001**, *86*, 858–861.
12. Fishman, D. A.; Revcolevschi, A.; van Loosdrecht, P. H. M. Exciton Dynamics in Cuprous Oxide. *Phys. Status Solidi C* **2006**, *3*, 2469–2472.
13. Jiang, X.; Herricks, T.; Xia, Y. CuO Nanowires Can Be Synthesized by Heating Copper Substrates in Air. *Nano Lett.* **2002**, *2*, 1333–1338.
14. Siegfried, M. J.; Choi, K.-S. Elucidating the Effect of Additives on the Growth and Stability of $Cu_2O$ Surfaces *via* Shape Transformation of Pre-Grown Crystals. *J. Am. Chem. Soc.* **2006**, *128*, 10356–10357.
15. White, B.; Yin, M.; Hall, A.; Le, D.; Stolbov, S.; Rahman, T.; Turro, N.; O'Brien, S. Complete CO Oxidation over $Cu_2O$ Nanoparticles Supported on Silica Gel. *Nano Lett.* **2006**, *6*, 2095–2098.
16. Mor, G. K.; Varghese, O. K.; Wilke, R. H. T.; Sharma, S.; Shankar, K.; Latempa, T. J.; Choi, K.−S.; Grimes, C. A. p-Type Cu−Ti−O Nanotube Arrays and Their Use in Self-Biased Heterojunction Photoelectrochemical Diodes for Hydrogen Generation. *Nano Lett.* **2008**, *8*, 1906–1911.
17. Gou, L.; Murphy, C. J. Solution-Phase Synthesis of $Cu_2O$ Nanocubes. *Nano Lett.* **2003**, *3*, 231–234.
18. Cao, H.; Qian, X.; Zai, J.; Yin, J.; Zhu, Z. Conversion of $Cu_2O$ Nanocrystals into Hollow $Cu_{2-x}Se$ Nanocages with the Preservation of Morphologies. *Chem. Commun.* **2006**, 4548–4550.
19. Siegfried, M. J.; Choi, K.-S. Electrochemical Crystallization of Cuprous Oxide with Systematic Shape Evolution. *Adv. Mater.* **2004**, *16*, 1743–1746.
20. Wang, W.; Wang, G.; Wang, X.; Zhan, Y.; Liu, Y.; Zheng, C. Synthesis and Characterization of $Cu_2O$ Nanowires by a Novel Reduction Route. *Adv. Mater.* **2002**, *14*, 67–69.

21. Chang, Y.; Teo, J. J.; Zeng, H. C. Formation of Colloidal CuO Nanocrystallites and Their Spherical Aggregation and Reductive Transformation to Hollow $Cu_2O$ Nanospheres. *Langmuir* **2005**, *21*, 1074–1079.
22. Park, J. C.; Kim, J.; Kwon, H.; Song, H. Gram-Scale Synthesis of $Cu_2O$ Nanocubes and Subsequent Oxidation to CuO Hollow Nanostructures for Lithium-Ion Battery Anode Materials. *Adv. Mater.* **2009**, *21*, 803–807.
23. Teo, J. J.; Chang, Y.; Zeng, H. C. Fabrications of Hollow Nanocubes of $Cu_2O$ and Cu *via* Reductive Self-Assembly of CuO Nanocrystals. *Langmuir* **2006**, *22*, 7369–7377.
24. Switzer, J. A.; Hung, C.-J.; Huang, L.-Y.; Switzer, E. R.; Kammler, D. R.; Golden, T. D.; Bohannan, E. W. Electrochemical Self-Assembly of Copper/Cuprous Oxide Layered Nanostructures. *J. Am. Chem. Soc.* **1998**, *120*, 3530–3631.
25. Lu, C.; Qi, L.; Yang, J.; Wang, X.; Zhang, D.; Xie, J.; Ma, J. One-Pot Synthesis of Octahedral $Cu_2O$ Nanocages *via* a Catalytic Solution Route. *Adv. Mater.* **2005**, *17*, 2562–2567.
26. Li, J.; Shi, Y.; Cai, Q.; Sun, Q.; Li, H.; Chen, X.; Wang, X.; Yan, Y.; Vrieling, E. G. Patterning of Nanostructured Cuprous Oxide by Surfactant-Assisted Electrochemical Deposition. *Cryst. Growth Des.* **2008**, *8*, 2652–2659.
27. Bradley, J.-C.; Chen, H.-M.; Crawford, J.; Eckert, J.; Ernazarova, K.; Kurzeja, T.; Lin, M.; McGee, M.; Nadler, W.; Stephens, S. G. Creating Electrical Contacts between Metal Particles Using Directed Electrochemical Growth. *Nature* **1997**, *389*, 268–271.
28. Wu, C.-K.; Yin, M.; O'Brien, S.; Koberstein, J. T. Quantitative Analysis of Copper Oxide Nanoparticle Composition and Structure by X-ray Photoelectron Spectroscopy. *Chem. Mater.* **2006**, *18*, 6054–6058.
29. Yu, Z. Q.; Wang, C. M.; Engelhard, M. H.; Nachimuthu, P.; McCready, D. E.; Lyubinetsky, I. V.; Thevuthasan, S. Epitaxial Growth and Microstructure of $Cu_2O$ Nanoparticle/Thin Films on $SrTiO_3$(100). *Nanotechnology* **2007**, *18*, 115601-5.
30. Balamurugan, B.; Mehta, B. R.; Shivaprasad, S. M. Surface-Modified CuO Layer in Size-Stabilized Single-Phase $Cu_2O$ Nanoparticles. *Appl. Phys. Lett.* **2001**, *79*, 3176–3178.
31. Sze, S. M. *Physics of Semiconductor Devices*, 2nd ed.; Wiley-Interscience: New York, 1981.
32. Xiang, A.; Wohlmuth, W.; Fay, P.; Kang, S.-M.; Adesida, I. Modeling of InGaAs MSM Photodetector for Circuit-Level Simulation. *J. Lightwave Technol.* **1996**, *14*, 716–723.
33. Carbone, A.; Mazzetti, P.; Rossi, F. Low-Frequency Photocurrent Noise in Semiconductors: Effect of Nonlinear Current−Voltage Characteristics. *Appl. Phys. Lett.* **2001**, *78*, 2518–2520.
34. Chui, C. O.; Okyay, A. K.; Saraswat, K. C. Effective Dark Current Suppression with Asymmetric MSM Photodetectors in Group IV Semiconductors. *IEEE Photon. Technol. Lett.* **2003**, *15*, 1585–1587.
35. Ng, T. N.; Silveira, W. R.; Marohn, J. A. Dependence of Charge Injection on Temperature, Electric Field, and Energetic Disorder in an Organic Semiconductor. *Phys. Rev. Lett.* **2007**, *98*, 066101-4.
36. Nakajima, K.; Iida, T.; Sugimoto, K.-I.; Kan, H.; Mizushima, Y. Properties and Design Theory of Ultrafast GaAs Metal−Semiconductor−Metal Photodetector with Symmetrical Schottky Contacts. *IEEE Trans. Electron Dev.* **1990**, *37*, 31–35.